Research Article Vol. 31, No. 3 / 30 Jan 2023 / Optics Express 4268
Optics EXPRESS

Chip-based SBS for image rejection in a broadband microwave photonic mixer

LUKE MCKAY,[1,2] CHOON KONG LAI,[1,2] NICHOLAS J. ATHANASIOS,[1,2] DUK-YONG CHOI,[3] STEPHEN J. MADDEN,[3] BENJAMIN J. EGGLETON,[1,2] AND MORITZ MERKLEIN[1,2,*]

[1]*The University of Sydney Nano Institute (Sydney Nano), The University of Sydney, Sydney, NSW, 2006, Australia*
[2]*Institute of Photonics and Optical Science (IPOS), School of Physics, The University of Sydney, Sydney, NSW, 2006, Australia*
[3]*Laser Physics Centre, The Australian National University, Canberra, ACT, 2601, Australia*
[*]*moritz.merklein@sydney.edu.au*

Abstract: Microwave photonics offers a promising solution for frequency converting microwave signals, however, demonstrations so far have either been bulky fibre implementations or lacked rejection of interfering image signals. Here, we demonstrate the first microwave photonic mixer with image rejection of broadband signals utilising chip-based stimulated Brillouin scattering and interferometry. We demonstrate frequency down-conversion of carrier frequencies ranging from 10 GHz-16 GHz, ultra-high image rejection for a single tone of up to 70 dB, and 100 MHz and 400 MHz wide analogue signals with 28.5 dB and 16 dB image rejection, respectively. Furthermore, we down-convert 200 Mb/s quadrature-phase-shift keying signals with an error vector magnitude as low as -9.6 dB when simultaneously present interfering image signals are suppressed by the mixer.

1. Introduction

Frequency mixers are essential building blocks of radio frequency (RF) front-ends for down-converting RF signals to low frequencies that can be processed by electronic analog to digital converts (ADCs) and are used in wireless communications, radar, satellite payloads as well as other applications [1]. Modern electrical approaches to frequency down-conversion mixers have limited operating frequency, tunability and are susceptible to electromagnetic interference [1,2]. Desirably, frequency mixers should be broadband, linear, i.e. have a high spurious free dynamic range (SFDR), and high-conversion gain. Additionally, as the electromagnetic spectrum is becoming increasingly crowded and congested unwanted RF signals at the image frequency, i.e. signals with the same frequency separation to the local oscillator as the signal of interest should not be down-converted. Hence, the ideal frequency down-converter will have deep image rejection to reduce the effect of signal interference and ensure signal integrity is retained. Traditional RF mixers rely on multiple cascaded down-conversion stages with fixed intermediate filters to remove the image component but this processes is noisy, introduces jitter, and increases the overall footprint [1].

Microwave photonics (MWP) provides a promising solution as it inherently offers wide operation frequency, tunability, immunity to electromagnetic interference, and the potential to greatly reduce size, weight and power (SWaP) consumption via photonic integration [2–4]. High performance frequency mixing was achieved in fiber using stimulated Brillouin scattering (SBS) [5], which was also used to achieve image rejection [6,7], an important feature of frequency mixers in real-world scenarios. Other fiber optic MWP mixers with image rejection were using the Hartley architecture [8–11], polarization [12–14], and asymmetric Mach–Zehnder

#482871 https://doi.org/10.1364/OE.482871
Journal © 2023 Received 8 Dec 2022; accepted 27 Dec 2022; published 20 Jan 2023

Optics EXPRESS

interferometers [15] among other approaches. Many of these works have demonstrated broadband image rejection which is required for real-world applications [11,12,14,15].

However, fibre systems are bulky and can be sensitive to environmental fluctuations. Integrating the entire device into an on-chip platform does not only significantly improve SWaP characteristics [2] but also stability and performance.

Various integrated MWP mixers have been published [16–23] utilising e.g. frequency combs [19–21]. High levels of integration have been achieved, with a laser and a set of balanced photodetectors integrated into a silicon chip [16]. Frequency up and down-conversion has been demonstrated in [17] and broadband mixers have been used as up-converters [18] and in delay beam-forming networks [22]. On the other hand, an integrated MWP mixer with image rejection was recently demonstrated [23] utilising SBS gain and loss to break interferometric symmetry to provide 45 dB of image rejection for a narrowband continuous wave (CW) RF tone [23].

In this paper, we demonstrate for the first time an integrated frequency mixer that combines broadband capability with image rejection, so it is capable of down-converting real signals in noisy or congested RF environments. Image rejection is achieved with broadband SBS in an integrated chalcogenide waveguide combined with RF interferometry. We demonstrate frequency down-conversion of carrier frequencies operation range from 10 GHz-16 GHz and ultra-high image rejection for a single tone of up to 70 dB. Furthermore, we show 28.5 dB and 16 dB of image rejection over a signal bandwidth of 100 MHz and 400 MHz, respectively, and down-convert a 200 Mb/s Quadrature-phase-shift keying (QPSK) signal. We characterise the performance of the mixer and demonstrate a conversion gain of up to -1 dB for the broadband signals and prove that the proposed image rejection scheme improves link quality even when a significantly stronger image tone is present.

2. Principle

Figure 1 depicts the concept of image rejection for an MWP frequency mixer. The detected signal consists of multiple RF signals, RF_{sig} and RF_{img}, which are fed into the modulator as seen in Fig 1(a). The local oscillator (LO) is modulated upon the optical carrier with a second modulator

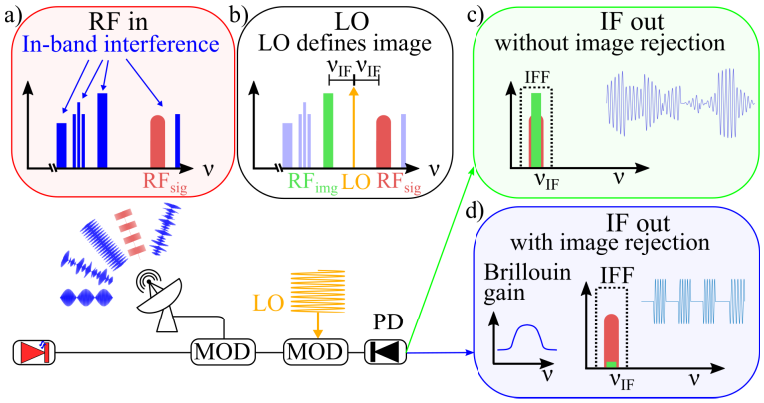

Fig. 1. Concept of frequency mixer with image rejection. a) A signal with in-band interference is fed into the mixer, the signal of interest RF_{sig} (red) and in-band interference (blue). b) One signal, the image (RF_{img}, shown in green) is equally separated from the local oscillator (LO). c) Without image rejection RF_{sig} and RF_{img} mix with the LO and down-convert to the same intermediate frequency (ν_{IF}). The output is then highly distorted and can not be improved with filtering. d) In the case of image rejection, stimulated Brillouin scattering (SBS) is used to isolate the signal of interest while attenuating the image component. The remaining down-converted signal is free of distortion. IFF: intermediate frequency filter. MOD: modulator. PD: photodetector.

Optics EXPRESS

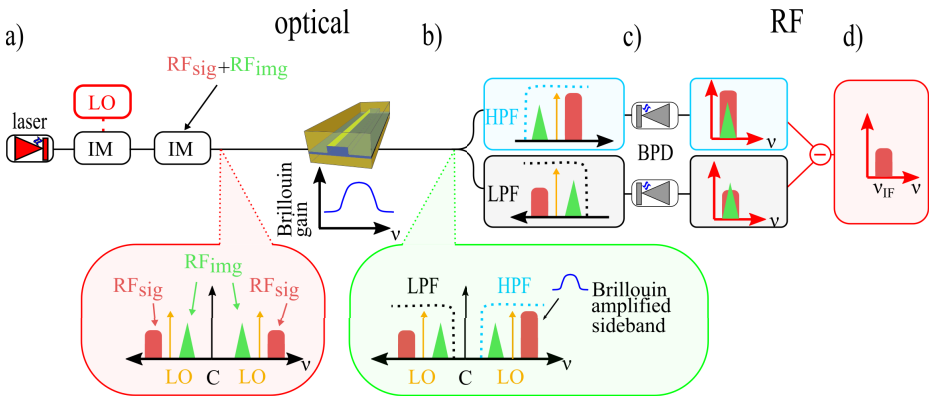

Fig. 2. Principle of the proposed image rejection scheme. a) The crowded spectrum is fed into the modulator, which encodes them on the optical carrier along with the LO. b) The optical signal then passes through the Chalcogenide waveguide, where the upper sideband component of RF_{sig} is amplified with SBS. c) The signal is split into two paths and filtered such that each output has one side of the optical carrier. Each path beats at the balanced photodetector. d) The components at the image frequency are symmetrical, so destructively interfere, leaving only the desired down-converted signal.

in series with the first one, as shown in Fig 1(b). RF signals at the same frequency spacing Δf on the upper and lower frequency side of the LO are down-converted to the same intermediate frequency (IF). This results in a superposition of both signal and image components which can lead to a highly distorted output signal that cannot be salvaged with further filtering as seen in Fig 1(c). However, when image rejection is implemented, e.g. by harnessing SBS, the IF signal corresponding to the image component RF_{img} is attenuated. Image rejection results in only the down-converted component from RF_{sig} at the output, shown in Fig 1(d).

The principle behind the image rejection process used in this work can be seen in Fig 2. The RF components RF_{sig} and RF_{img} are modulated with an intensity modulator on the optical carrier along with a LO as shown in Fig 2(a). The optical signal propagates through the chalcogenide chip and is then split into two paths. The lower path is filtered by a low pass filter (LPF) which selects the frequency components lower than the optical carrier. Similarly, the signal in the upper path selects frequencies higher than the optical carrier with a high pass filter (HPF) (The optical LPF and HPF are tunable optical filter (Alnair BVF-330CL) that offer a steep roll-off of 1500dB/nm and a minimum bandwidth of 30 pm). The end of each path feeds into a balanced photodetector (BPD). The resultant mixing products from each path are nominally identical and thus destructively interfere, which leads to a null output independent of the input signal.

SBS in a chalcogenide waveguide is then used to select the desired RF component and break the symmetry required for image rejection. Chalcogenide rib waveguides surrounded by a silica cladding have shown to achieve large Brillouin gain in a small footprint due to the strong opto-acoustic overlap, that leads to a large Brillouin gain coefficient, enabled by the simultaneous guidance of optical and acoustic modes in the small waveguide core [24–26]. Chip-based SBS offers many unique advantages for signal processing as it is an optically induced gain (loss) process with a narrow intrinsic linewidth in the tens of MHz. The width of the Brillouin gain (loss) and its center frequency can be tuned via the optical pump profile and offers a large degree of flexibility and reconfigurability that led to demonstrations of novel chip-based devices and applications [27–29].

In our mixer scheme, the SBS gain is applied to the component RF_{sig} on the upper sideband which amplifies the signal and applies a phase shift as shown in Fig 2(b). The optical signals

Optics EXPRESS

are then detected by a photodetector in each corresponding path of the BPD producing a down-converted IF copy of RF_{sig} and RF_{img}, as seen in Fig 2(c). The upper sideband component RF_{sig} has been amplified by SBS, so the corresponding IF signal in the electrical domain is larger than the IF signal generated from the lower sideband. The difference in amplitude and phase between the two components results in a down-converted copy of the IF signal at the output of the BPD. At the same time, the symmetry from the down-converted component of RF_{img} is maintained, as it was unaffected by SBS gain. The down-converted components from RF_{img} completely destructively interfere as the RF_{img} components in both the upper and lower sidebands are identical in both amplitude and phase. The output of the PD is then purely the down-converted output from RF_{sig} as seen in Fig 2(d).

3. Theory

The optical link consists of a single laser which is then injected into two cascaded Mach-Zehnder modulators (MZM). Both modulators are quadrature biased. The first modulator is driven by a local oscillator with signal $V_{LO}\sin(\omega_{LO}t)$. The electric field emerging from this modulator (MZM_1) is given as:

$$\begin{aligned} E_{MZM1} \approx\ & E_0[J_0(m_{LO})\exp(j\omega_c t) \\ & + J_1(m_{LO})\exp(j(\omega_c + \omega_{LO})t) + J_1(m_{LO})\exp(j(\omega_c - \omega_{LO})t) \\ & + J_2(m_{LO})\exp(j(\omega_c + 2\omega_{LO})t) + J_2(m_{LO})\exp(j(\omega_c - 2\omega_{LO})t)] \end{aligned} \tag{1}$$

where E_0 is the optical field incident on the modulator and harmonics larger than second order are ignored. The optical loss through the system is ignored, so the loss due to modulator bias voltages are also not considered. Here, m_{LO} is the modulation index for the local oscillator, J_n is the nth order Bessel function of the first kind, and ω_c is the frequency of the optical carrier. The output is then fed into the second modulator (MZM_2). MZM_2 is driven by both the signals RF_{sig} and RF_{img} given by $V_{sig}\sin(\omega_{sig}t)$ and $V_{img}\sin(\omega_{img}t)$, respectively. The electric field after MZM_2 is given by:

$$E_{out} = E_{MZM1} * E_{MZM2} \tag{2}$$

Expanding the above equation:

$$\begin{aligned} E_{out} \approx\ & E_{MZM1}[J_0(m_{sig})J_0(m_{img})\exp(j\omega_c t) \\ & + J_1(m_{sig})\exp(j(\omega_c + \omega_{RF_{sig}})t) + J_1(m_{sig})\exp(j(\omega_c - \omega_{RF_{sig}})t) \\ & + J_1(m_{img})\exp(j(\omega_c + \omega_{RF_{img}})t) + J_1(m_{img})\exp(j(\omega_c - \omega_{RF_{img}})t) \\ & + J_2(m_{sig})\exp(j(\omega_c + 2\omega_{RF_{sig}})t) + J_2(m_{sig})\exp(j(\omega_c - 2\omega_{RF_{sig}})t) \\ & + J_2(m_{img})\exp(j(\omega_c + 2\omega_{RF_{img}})t) + J_2(m_{img})\exp(j(\omega_c - 2\omega_{RF_{img}})t)] \end{aligned} \tag{3}$$

where harmonics greater than second order are ignored. m_{sig} and m_{img} are the signal and image modulation indices respectively. The optical signal at frequency ω_c at the output of MZM_1 is significantly stronger than any other component so only terms generated from this component by MZM_2 will be considered. At this point, Brillouin gain is applied to the fundamental component RF_{sig} in the upper sideband, and the signal is split into an upper and lower paths before being filtered in their respective paths. In the upper path the optical signal incident on the upper balanced photodector (UBPD) is given as:

$$\begin{aligned} E_{UBPD} \approx\ & G_B(\omega)J_0(m_{LO})J_1(m_{sig})\exp(j(\omega_c + \omega_{RF_{sig}})t) \\ & + J_0(m_{LO})J_1(m_{img})\exp(j(\omega_c + \omega_{RF_{img}})t) \\ & + J_1(m_{LO})\exp(j(\omega_c + \omega_{LO})t) \end{aligned} \tag{4}$$

Optics EXPRESS

The resulting photocurrents generated in the upper PD are:

$$\begin{aligned} I_{UBPD} \approx RP_r[&G_B(\omega)J_0(m_{LO})J_1(m_{sig})\cos((\omega_{RF_{sig}} - \omega_{LO})t) \\ &+ J_0(m_{LO})J_1(m_{img})\cos((\omega_{LO} - \omega_{RF_{img}})t) \\ &+ J_0(m_{LO})J_2(m_{img})\cos((\omega_{LO} - 2\omega_{RF_{img}})t) \\ &+ J_0(m_{LO})J_2(m_{sig})\cos((\omega_{LO} - 2\omega_{RF_{sig}})t)] \end{aligned} \tag{5}$$

where R is the responsivity of the photodetector and P_r is the power incident on the photodetector. Only the mixing products between RF_{LO} and the fundamental and first harmonic of RF_{sig} and between RF_{LO} and fundamental and first harmonic of RF_{img} are considered here. G_B is the Brillouin gain given by the following equation:

$$G_B(\omega) = \exp(\frac{G}{2}\frac{\Gamma_B^2}{4\Delta\omega^2 + \Gamma_B^2}) \tag{6}$$

The Brillouin gain is given in terms of the power dependent variable G. Note: this equation is described in terms of the electric field, hence the factor of $\frac{1}{2}$. In the above equation, Γ_B is the Brillouin linewidth, Ω_B is the Brillouin frequency shift, $\Delta\omega = \omega_p - \Omega_B - \omega$ is the offset frequency from the centre of the Brillouin response. The phase response is given by [30,31]:

$$\theta_{SBS}(\omega) = -G\Gamma_B\frac{\Delta\omega}{4\Delta\omega^2 + \Gamma_B^2} \tag{7}$$

where G is the Brillouin gain factor given by:

$$G = \frac{g_0}{A_0}P_p(0)L_{eff} \tag{8}$$

where g_0 is the gain coefficient of the medium, A_0 is the acousto-optic effective area, $P_p(0)$ is the pump power launched into the medium and L_{eff} is the effective length, calculated as:

$$L_{eff} = \frac{1}{\alpha}(1 - \exp(-\alpha L)) \tag{9}$$

where α is the attenuation coefficient and L is the physical length of the medium. The electric field experienced at the lower balanced photodetector (LBPD) is:

$$\begin{aligned} E_{UBPD} \approx\ &J_0(m_{LO})J_1(m_{sig})\exp(j(\omega_c - \omega_{RF_{sig}})t) \\ &+ J_0(m_{LO})J_1(m_{img})\exp(j(\omega_c - \omega_{RF_{img}})t) \\ &+ J_1(m_{LO})\exp(j(\omega_c - \omega_{LO})t) \end{aligned} \tag{10}$$

And generates the corresponding photcurrent at the output:

$$\begin{aligned} I_{LBPD} \approx RP_r[&J_0(m_{LO})J_1(m_{sig})\cos((\omega_{RF_{sig}} - \omega_{LO})t) \\ &+ J_0(m_{LO})J_1(m_{img})\cos((\omega_{LO} - \omega_{RF_{img}})t) \\ &+ J_0(m_{LO})J_2(m_{img})\cos((\omega_{LO} - 2\omega_{RF_{img}})t) \\ &+ J_0(m_{LO})J_2(m_{sig})\cos((\omega_{LO} - 2\omega_{RF_{sig}})t)] \end{aligned} \tag{11}$$

These two signals are converted to photocurrents and the LBPD is subtracted from the UPBD resulting in only the down-converted signal component I_{out}:

$$I_{out} \approx RP_r(G_B(\omega) - 1)J_0(m_{LO})J_1(m_{sig})\cos((\omega_{RF_{sig}} - \omega_{LO})t) \tag{12}$$

Optics EXPRESS

4. Experimental setup

A schematic of the experimental setup is depicted in Fig 3(a). A high power laser is split into two paths with a 90:10 splitter. The output of the 90% port is fed into an intensity modulator driven by the LO before continuing through a second intensity modulator which is driven by both the RF signal and image components. Both modulators are driven by RF amplifiers (ZVA-183-S+). The modulated waveform is amplified by an EDFA then passes through the integrated chalcogenide rib waveguide. The waveguide is composed of As_2S_3 and is 23 cm long, 2.4 µm wide, 960 nm tall, with an etch depth of 300 nm and is laid out in a spiral structure to reduce the footprint, as can be seen in Fig 3(b). The waveguide had a total insertion loss of 16.5 dB made up of propagation loss and coupling loss from the fibre-to-chip interface. The As_2S_3 waveguide is either coupled with tapered fibre or with on-chip tapers. The chip-based approach uses vertical tapers on a germanosilicate waveguide section at both facets [32] and is coupled utilising an optical stage as shown in Fig 3(c). The germanosilicate waveguide section at the end facet is mode matched to ultra-high-numerical-aperture fibre and hence improves coupling efficiency and reduces back-reflections from the chip-fiber interface [32]. The signal continues after the chip to a circulator which routes it the BPD.

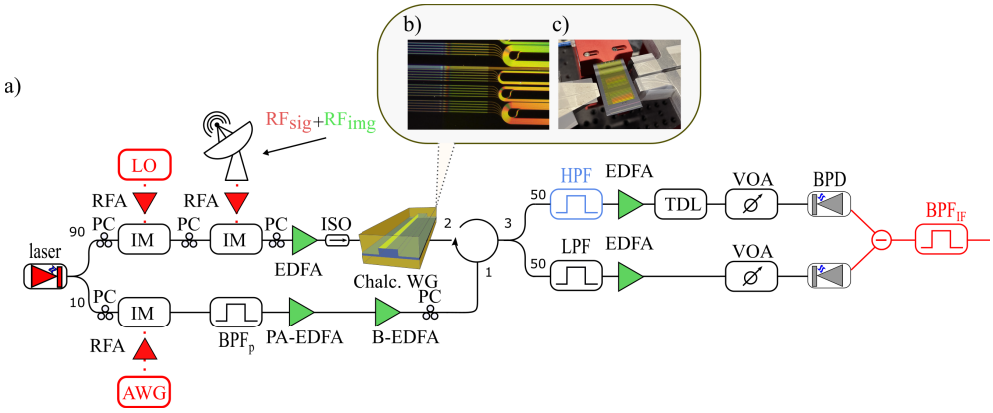

Fig. 3. a) Experimental setup. b) Image of the As_2S_3 chip as seen through a microscope. c) The chip on the optical stage. LO: local oscillator; IM: intensity modulator; BPF: bandpass filter; Chalc. WG: chalcogenide waveguide; AWG: arbitrary waveform generator; BPD: balanced photodetector; VOA: Variable optical attenuator; ISO: isolator; PC: polarisation controller; HPF: high pass filter; LPF: low pass filter; EDFA: erbium-doped fibre amplifier (B: boost; PA: pre-amplifier); TDL: tunable delay line; RFA: RF amplifier; RF_{sig}: RF signal; RF_{img}: RF image.

In the lower path, after the 10% port, the output is passed through an intensity modulator driven by an arbitrary waveform generator (AWG) and RF amplifier (SHF L806). The AWG generates the pump profile which selects the frequency operation range and signal bandwidth to be down-converted and is frequency shifted relative to the signal of interest by the Brillouin frequency shift of 7.7 GHz as seen in Fig 3(a). After the intensity modulator a bandpass filter is used to select the frequency shifted sideband and a low-noise pre-amplifier and a boost amplifier are used to amplify the pump power (a low noise EDFA pre-amplifier was used in conjunction with a high-power boost EDFA in order to reduce the combined noise figure. The noise figure of a chain of amplifiers is dominated by the noise figure of the first component in the link according to the Friis' formula for noise).

The pump waveform continues through the circulator before counter-propagating the optical carrier with the LO and the RF signal and image components from the upper path through

Optics EXPRESS

the chalcogenide waveguide. The counter-propagating pump interacts with the upper sideband component of RF_{sig}, amplifying it and inducing a phase shift. The optical carrier, the amplified sideband along with other spectral components then pass through the circulator and into a 50:50 splitter. Each arm after the 50:50 splitter consists of a bandpass filter, which fills the role of the HPF and LPF, respectively, EDFAs then amplify the optical signals. Variable optical attenuators (VOA) were placed after the EDFAs to fine control the amplitude of the signals and to ensure complete destructive interference. A tunable delay line (TDL) was placed in the upper path to ensure that optical path lengths are matched so the IF components are 180° out of phase. These signals then continue down their respective paths to be detected by the BPD. An RF bandpass filter (BPF_{IF}) with a bandwidth covering 1.15 GHz to 3.4 GHz was used after the output of the BPD so only the IF component is present (the RF bandpass filter function was achieved by cascading a high pass filter, VHF-1080+, and a lowpass filter,VLF-3400+).

5. Results

Initially, the narrowband performance of the mixer was characterised. A single narrowband RF tone was down-converted from 12 GHz to 2 GHz, via an LO at 10 GHz and with an 8 GHz image of equal amplitude to the signal (Fig. 4). The chalcogenide waveguide used for the following measurements was coupled with tapered fibres. First, the Brillouin gain of the on-chip waveguide was measured to characterise the system. For that purpose the LO was disconnected and the VOA in the lower path was closed so no destructive interference could occur. A single RF tone from the AWG (Keysight M8195A) generated a sideband in the lower path in Fig. 3(a) which acts as the Brillouin pump. The optical pump had a 7.7 GHz Brillouin frequency shift relative to the RF_{sig}, and when turned on, 20.1 dBm of optical power generated 5 dB of SBS gain.

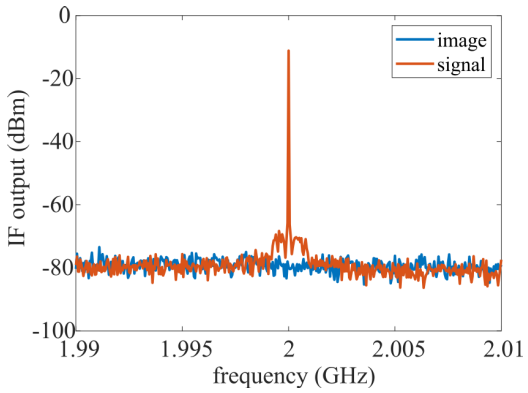

Fig. 4. The signal (orange) is down-converted from 12 GHz to 2 GHz with a conversion gain of -5 dB using 5 dB of SBS gain. The 8 GHz image component (blue) is down-converted to the same frequency, however it is at least 70 dB weaker.

The setup was then configured as an image rejection mixer. A 10 GHz LO was connected and both photodetectors of the BPD were used with the two optical paths balanced to produce a high level of RF interference across the entire IF band. The LO was set to have a power of -7 dBm, which is used for all the following experiments where the LO is required. RF_{img} was injected into the modulator and SBS gain was applied, the resulting spectrum was recorded after the BPD with a spectrum analyser (SA) (Field Fox N9952A), as shown in Fig. 4 in blue. To determine the amplitude of the signal component, RF_{img} was disconnected and RF_{sig} was then injected into the modulator with a centre frequency of 12 GHz, while the pump remained unchanged. The resulting spectrum was recorded and is shown in orange in Fig. 4. A total of 70 dB of image rejection was recorded for a single tone, with a conversion gain of -5 dB.

Optics EXPRESS

The experiment was then repeated over a wide frequency range to demonstrate frequency tunability of the MWP mixer. The following measurements use a chalcogenide waveguide with on-chip germanosilicate tapers with identical dimensions as previously and 12.3 dB of total optical loss. The waveguide produced 14.2 dB of Brillouin gain for 22 dBm of optical pump power. Fig. 5 shows the corresponding image rejection (blue) and conversion gain (orange) for RF signals covering a frequency range between 10-16 GHz down-converted to the same 2 GHz IF. We note that the operation frequency of this mixer is not limited to this particular frequency range and higher and lower frequencies can be down-converted without any expected degradation in performance. The higher frequency limit is set by the used electro-optic modulator and the RF source to generate the LO. On the lower frequency side, the limitation of the current proof-of-principle is set by the optical filters used in the setup, however, those filters are not strictly necessary in future architectures, as discussed in section 6.

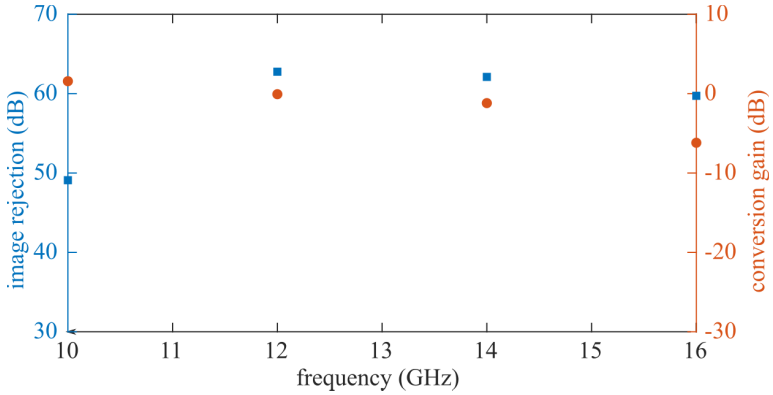

Fig. 5. A single tone was down-converted over a wide frequency range with 14.2 dB of SBS gain generated from 22 dBm of pump power. The image rejection is shown in blue and the corresponding conversion gain is shown in orange.

The mixer was then configured to operate in a broadband regime. Again, before down-converting RF_{sig}, the Brillouin gain spectrum was characterised with a pump-probe measurement. A 100 MHz bandwidth signal was fed into the system with a centre frequency of 12 GHz and only one arm of the BPD was used to avoid destructive interference. The normalised output is plotted in Fig. 6(a). The broadband Brillouin pump was then configured with a centre frequency of 19.7 GHz, 7.7 GHz above the probe frequency, and was set to 25.3 dBm of optical power. This resulted in 8.4 dB of broadband Brillouin gain, plotted in orange in Fig. 6(a).

The frequency mixer was then configured to down-convert a 12 GHz signal with 100 MHz bandwidth to demonstrate broadband image rejection. The LO was enabled and set to 10 GHz to generate a 2 GHz IF output at the BPD. Initially, the amplitude of the image component was measured. The VOA in the lower path was opened so both BPD detectors were active. The Brillouin pump was enabled and the amplitude of the image component was determined by feeding in an 8 GHz signal. Small adjustments to the optical path length were made to compensate for phase errors in the interfering component. In addition, adjustments to the VOA were made to control the amplitude of the interfering phasors until a minimum amplitude at the output was achieved. This corresponded to a maximum level of destructive interference (blue trace in Fig. 6(b)).The maximum image rejection depends on the degree of destructive interference, i.e., how well the signal amplitudes and phases are balanced and the SBS gain. The 12 GHz signal was then injected into the modulator and was 28.5 dB larger than the image component (orange trace in Fig. 6(b)).

Optics EXPRESS

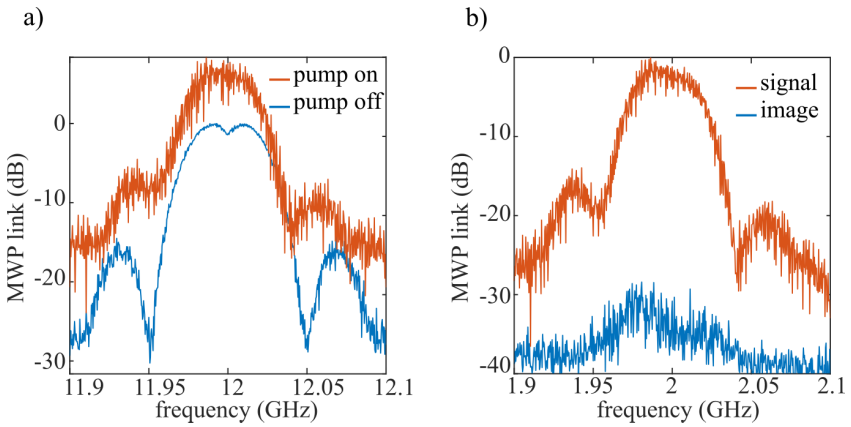

Fig. 6. a) 100 MHz broadband gain profile. Blue: no Brillouin gain applied (normalised to 0 dB); Orange: signal with 8.4 dB Brillouin gain. b) Down-converted 100 MHz wide signal with 28.5 dB image rejection and -1 dB of conversion gain. Orange: signal; blue: image.

To demonstrate tunability of the signal bandwidth and operation frequency range, the above experiments were repeated with a 400 MHz bandwidth signal, this time with a carrier frequency of 11 GHz. The optical spectrum without Brillouin gain or interference is plotted in blue in Fig. 7(a) and normalised to 0 dB. The broadband pump is then applied with a centre frequency of 18.7 GHz with 25.5 dBm of optical power. This generated 4 dB of broadband Brillouin gain which is plotted in orange in Fig. 7(a). The experimental setup is again configured as a frequency mixer and the LO is set to operate at 9 GHz, to achieve a 2 GHz IF output. Image rejection was measured with the signal frequency set to 11 GHz (orange trace in Fig. 7(b) and the corresponding image frequency at 7 GHz, which is shown in blue in Fig. 7(b). 16 dB of broadband image rejection was recorded.

Next, a 12 GHz 200 Mb/s QPSK signal is down-converted simultaneously with an 8 GHz image component present. The image signal consists of a frequency comb which is 10 dB larger than RF_{sig}. It is important to characterise the performance of the mixer with the signal of interest

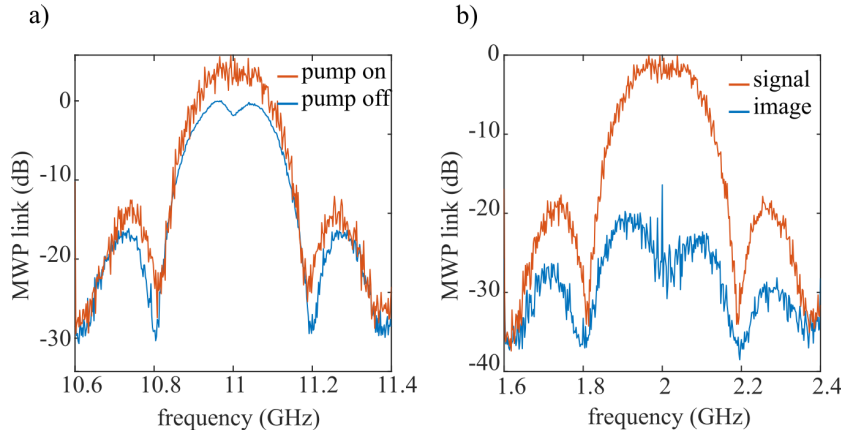

Fig. 7. a) 400 MHz broadband gain profile. Blue: no Brillouin gain applied (normalised to 0 dB); Orange: signal with 4 dB Brillouin gain. b) Down-converted 400 MHz wide signal with 16 dB image rejection. Orange: signal; blue: image.

Optics EXPRESS

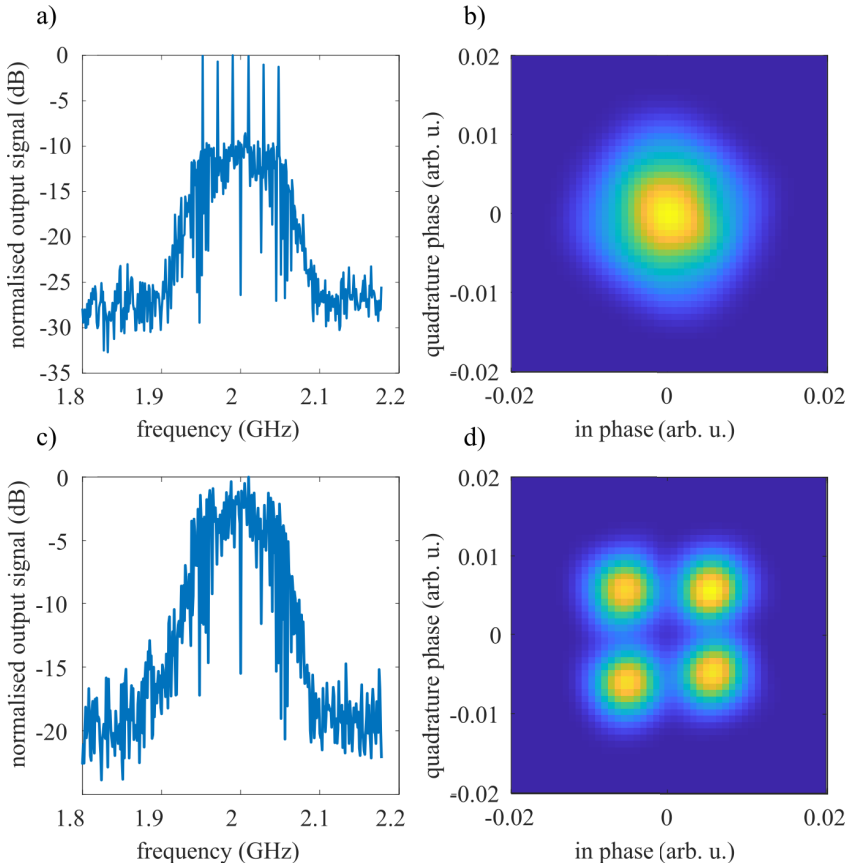

Fig. 8. A 200 Mb/s QPSK signal is down-converted simultaneously with an image component that consists of a frequency comb. The image is 10 dB larger than the signal. a) The combined down-converted spectrum of the QPSK signal and the frequency comb. b) Corresponding constellation diagram detected at the output. There was no meaningful data detected after demodulation. c) Down-converted spectrum consisting of both the signal and image after image rejection with 2.5 dB of broadband Brillouin gain has been applied. d) Corresponding constellation diagram with an EVM of -9.6 dB.

and the image signal present at the same time as this is how the mixer would operate in a crowded and congested electromagnetic environment. The combined spectrum of the down-converted signal and image are shown without image rejection in Fig. 8(a). Without image rejection, both RF_{sig} and RF_{img} down-convert to the same IF frequencies and produce the constellation diagram shown in Fig. 8(b). The signal is completely distorted and no meaningful signal can be recovered at the output of the mixer. 2.5 dB of broadband SBS gain is then applied and both BPDs are used and balanced so that image rejection is present. This results in the spectrum shown in Fig. 8(c). The tones from the frequency comb are suppressed below the amplitude of the broadband signal. The down-converted signal is then demodulated and plotted in a constellation diagram, which is shown in Fig. 8(d). The constellation diagram has 4 distinct quadrants with a recorded Error Vector Magnitude (EVM) of -9.6 dB for a signal with a data rate of 200 Mb/s. The down-conversion from 2 GHz to baseband was done in software, with a bandpass filter applied around the signal before the software oscillator is applied. An additional low-pass software filter is applied to the baseband signal before the constellation diagram is plotted.

Optics EXPRESS

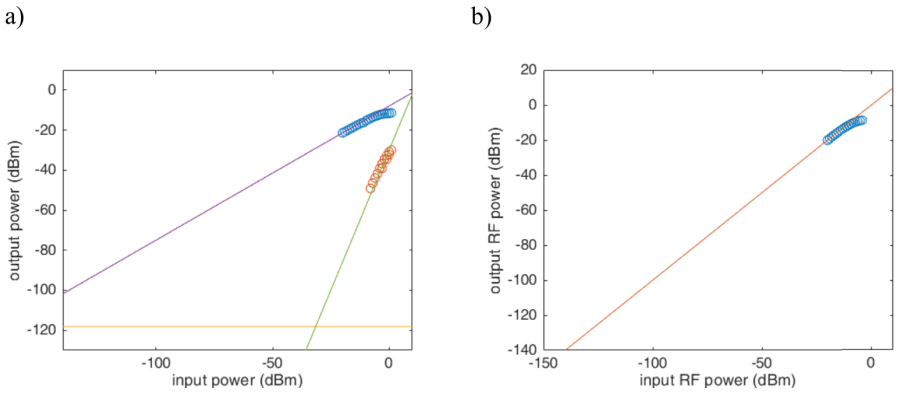

Fig. 9. a) The spurious free dynamic range (SFDR) of the mixer of 89.2 dBHz$^{2/3}$ with a noise floor was -118.2 dBm/Hz. b) Compression point measurement of the mixer shows a 1 dB compression point for an output power of -12 dBm.

The dynamic range of the mixer was then measured. To measure the SFDR two RF sources were used to inject two RF tones into the mixer with a frequency separation of 10 MHz. The SFDR of the mixer was measured to be 89.2 dBHz$^{2/3}$ and can be seen in Fig. 9(a). The second RF source was removed and the output 1 dB compression point was measured to be -12 dBm as seen in Fig. 9(b). The noise floor was -118.2 dBm/Hz, which is relatively high and mainly caused by the losses in the link and the high levels of amplification to compensate for said losses.

6. Discussion

During the initial setup, the optical path-lengths after the 50:50 splitter were matched and a large amount of destructive interference was present over the entire frequency range of the mixer. The amplitude and phase changes brought about by broadband Brillouin gain would be the only contribution to breaking the signal symmetry. However, in the above experiments, the HPF applies a strong dispersive phase-slope around the passband due to the steep filtering required to remove the pump back-reflection. It was critical to remove the pump back-reflection as it would induce gain competition in the erbium-doped fibre pre-amplifier before the balanced detector. This gain competition would induce a significant quantity of noise. An unfortunate consequence of the dispersion is that it reduced the destructive interference at the image frequency. To compensate for this, the TDL was adjusted until interference was achieved. This had the consequence of forming an RF two-tap filter (TTF), similar to the work by Lipkowitz et al. [15]. This is significant as the TTF has the effect of reducing the system flexibility and is thus undesirable.

The relative contribution of the TTF diminishes as the level of Brillouin gain is increased. Increasing the effective length of the chalcogenide waveguide would therefore improve performance as it would provide more Brillouin gain for any given level of optical pump power, provided the gain is not saturated. The issue of back-reflection could be reduced by further optimising the taper to bypass the back-reflection which in turn would reduce filtering requirements. Future work could see the entire device integrated into a hybrid on-chip device [33], which would completely bypass the large index contrasts between single-mode fibre and chalcogenide waveguides potentially further reducing back-reflections. Integration would also reduce the footprint as well as power consumption while increasing system stability.

Additionally, the time domain signal shown in Fig. 8(d) was partially distorted due to a limited pump-probe overlap. For broadband operation, pump profiles consisting of equally spaced tones

Optics EXPRESS

tend to generate pulses in the time domain. These time domain pulses then lead to temporally varying levels of Brillouin amplification. In long waveguides such as single-mode fibre, the probe interacts with many such pulses and experiences an averaging effect. However, in short waveguides where there is limited pump-probe overlap, it can lead to temporal distortions that are seen in an increase of the noise when the pump is turned on. However, Fig. 8 shows that the mixer is capable of improving the quality of a down-converted link despite this distortion. In summary, the mixer performance would greatly increase with larger SBS gain, as well as lower waveguide losses that will allow longer waveguides and remove the need for extra EDFAs that add noise to the current system. Higher levels of integration would reduce reflections from interfaces which would remove the need of narrowband filters and again increase overall performance metrics. Electro-optic modulator with a lower V_π would further improve the link gain.

7. Conclusion

In this work, we demonstrated an MWP mixer that is able to down-convert broadband signals while at the same time rejecting image frequency signals using chip-based SBS. The mixer is capable of operating over broad operating frequency ranges, here demonstrated for carrier frequencies from 10 GHz to 16 GHz, while allowing on-the-fly reconfiguration with deep image rejection capabilities of up to 70 dB for a single RF tone and 28.5 dB and 16 dB for broadband 100 MHz and 400 MHz signals, respectively. We demonstrated a high conversion gain of up to -1 dB and down-convert a 200 Mb/s QPSK signal while maintaining signal integrity in the presence of strong image signals that are suppressed in the down-conversion process. This work paves the way for a fully integrated reconfigurable MWP mixer with image rejection for use in highly versatile commercial applications, such as e.g. RF front-ends and phased array antennas for wireless communication and Radar applications.

Funding. Australian Research Council (DP220101431, LP170100112); Office of Naval Research Global (N62909-18-1-2013); U.S. Air Force (FA2386-16-1-4036).

Acknowledgements. We would like to thank Richard DeSalvo and his team at L3Harris for their invaluable discussions. This work used the ACT node of the NCRIS-enabled Australian National Fabrication Facility (ANFF-ACT).

Disclosures. The authors declare no conflict of interest.

Data availability. Data underlying the results presented in this paper are not publicly available at this time but may be obtained from the authors upon reasonable request.

References

1. Z. Tang, Y. Li, J. Yao, and S. Pan, "Photonics-based microwave frequency mixing: Methodology and applications," Laser Photonics Rev. **14**(1), 1800350 (2020).
2. D. Marpaung, J. Yao, and J. Capmany, "Integrated microwave photonics," Nat. Photonics **13**(2), 80–90 (2019).
3. A. J. Seeds and K. J. Williams, "Microwave photonics," J. Lightwave Technol. **24**(12), 4628–4641 (2006).
4. J. Capmany and D. Novak, "Microwave photonics combines two worlds," Nat. Photonics **1**(6), 319–330 (2007).
5. E. H. W. Chan and R. A. Minasian, "High conversion efficiency microwave photonic mixer based on stimulated Brillouin scattering carrier suppression technique," Opt. Lett. **38**(24), 5292–5295 (2013).
6. X. Kong, Y. Yu, H. Tang, and X. Zhang, "Microwave photonic image-reject mixer based on a tunable microwave photonic filter with high rejection," IEEE Photonics J. **10**(6), 1–11 (2018).
7. C. B. Albert, C. Huang, and E. H. W. Chan, "Brillouin-assisted notch filtering based all-optical image rejection mixer," IEEE Photonics J. **11**(2), 1–12 (2019).
8. H. Ogawa and H. Kamitsuna, "Fiber optic microwave links using balanced laser harmonic generation, and balanced/image cancellation laser mixing," IEEE Trans. Microwave Theory Tech. **40**(12), 2278–2284 (1992).
9. L. Chao, C. Wenyue, and J. Shiang, "Photonic mixers and image-rejection mixers for optical SCM systems," IEEE Trans. Microwave Theory Tech. **45**(8), 1478–1480 (1997).
10. D. Zhu, W. Chen, and S. Pan, "Photonics-enabled balanced Hartley architecture for broadband image-reject microwave mixing," Opt. Express **26**(21), 28022–28029 (2018).
11. W. Chen, D. Zhu, J. Liu, and S. Pan, "Multi-Band RF Transceiver Based on the Polarization Multiplexed Photonic LOs and Mixers," IEEE J. Sel. Top. Quantum Electron. **27**(2), 1–9 (2021).
12. Z. Tang and S. Pan, "Image-reject mixer with large suppression of mixing spurs based on a photonic microwave phase shifter," J. Lightwave Technol. **34**(20), 4729–4735 (2016).

Optics EXPRESS

13. P. Li, W. Pan, X. Zou, B. Lu, L. Yan, and B. Luo, "Image-free microwave photonic down-conversion approach for fiber-optic antenna remoting," IEEE J. Quantum Electron. **53**(4), 1–8 (2017).
14. D. Shan, A. Wen, W. Zhai, X. Li, W. Zhang, and Z. Tu, "Filter-free image-reject microwave photonic downconverter based on cascaded modulators," Appl. Opt. **58**(13), 3432–3437 (2019).
15. S. T. Lipkowitz, T. U. Horton, and T. E. Murphy, "Wideband microwave electro-optic image rejection mixer," Opt. Lett. **44**(19), 4710–4713 (2019).
16. S. Jin, L. Xu, V. Rosborough, J. Klamkin, and Y. Li, "RF frequency mixer photonic integrated circuit," IEEE Photonics Technol. Lett. **28**(16), 1771–1773 (2016).
17. C. G. Bottenfield and S. E. Ralph, "High-performance fully integrated silicon photonic microwave mixer subsystems," J. Lightwave Technol. **38**(19), 5536–5545 (2020).
18. K. Van Gasse, J. Verbist, H. Li, G. Torfs, J. Bauwelinck, and G. Roelkens, "Silicon photonics radio-over-fiber transmitter using GeSi EAMs for frequency up-conversion," IEEE Photonics Technol. Lett. **31**(2), 181–184 (2019).
19. T. Zhang, W. Pan, X. Zou, B. Luo, L. Yan, X. Liu, and B. Lu, "High-spectral-efficiency photonic frequency down-conversion using optical frequency comb and SSB modulation," IEEE Photonics J. **5**(2), 7200307 (2013).
20. J. Liao, X. Zheng, S. Li, H. Zhang, and B. Zhou, "High-efficiency microwave photonic harmonic down-conversion with tunable and reconfigurable filtering," Opt. Lett. **39**(23), 6565–6568 (2014).
21. X. Xu, J. Wu, M. Tan, T. G. Nguyen, S. T. Chu, B. E. Little, R. Morandotti, A. Mitchell, and D. J. Moss, "Broadband microwave frequency conversion based on an integrated optical micro-comb source," J. Lightwave Technol. **38**(2), 332–338 (2020).
22. V. C. Duarte, J. G. Prata, C. F. Ribeiro, R. N. Nogueira, G. Winzer, L. Zimmermann, R. Walker, S. Clements, M. Filipowicz, M. Napierała, T. Nasiłowski, J. Crabb, M. Kechagias, L. Stampoulidis, J. Anzalchi, and M. V. Drummond, "Modular coherent photonic-aided payload receiver for communications satellites," Nat. Commun. **10**(1), 1984 (2019).
23. Z. Zhu, D.-Y. Choi, S. J. Madden, B. J. Eggleton, and M. Merklein, "High-conversion-gain and deep-image-rejection Brillouin chip-based photonic RF mixer," Opt. Lett. **45**(19), 5571–5574 (2020).
24. R. Pant, C. G. Poulton, D.-Y. Choi, H. Mcfarlane, S. Hile, E. Li, L. Thevenaz, B. Luther-Davies, S. J. Madden, and B. J. Eggleton, "On-chip stimulated Brillouin scattering," Opt. Express **19**(9), 8285–8290 (2011).
25. C. G. Poulton, R. Pant, and B. J. Eggleton, "Acoustic confinement and stimulated Brillouin scattering in integrated optical waveguides," J. Opt. Soc. Am. B **30**(10), 2657–2664 (2013).
26. B. J. Eggleton, C. G. Poulton, P. T. Rakich, M. J. Steel, and G. Bahl, "Brillouin integrated photonics," Nat. Photonics **13**(10), 664–677 (2019).
27. D. Marpaung, B. Morrison, M. Pagani, R. Pant, D.-Y. Choi, B. Luther-Davies, S. J. Madden, and B. J. Eggleton, "Low-power, chip-based stimulated Brillouin scattering microwave photonic filter with ultrahigh selectivity," Optica **2**(2), 76 (2015).
28. M. Merklein, A. Casas-Bedoya, D. Marpaung, T. F. S. Buttner, M. Pagani, B. Morrison, I. V. Kabakova, and B. J. Eggleton, "Stimulated Brillouin Scattering in Photonic Integrated Circuits: Novel Applications and Devices," IEEE J. Sel. Top. Quantum Electron. **22**(2), 336–346 (2016).
29. L. McKay, M. Merklein, A. Choudhary, Y. Liu, M. Jenkins, C. Middleton, A. Cramer, A. Chilton, J. Devenport, K. Vu, D. Y. Choi, P. Ma, S. J. Madden, R. Desalvo, and B. J. Eggleton, "Broadband Brillouin Phase Shifter Utilizing RF Interference: Experimental Demonstration and Theoretical Analysis," J. Lightwave Technol. **38**(14), 3624–3636 (2020).
30. M. Pagani, D. Marpaung, and B. J. Eggleton, "Ultra-wideband microwave photonic phase shifter with configurable amplitude response," Opt. Lett. **39**(20), 5854–5857 (2014).
31. R. W. Boyd, *Nonlinear optics* (Academic Press, Amsterdam, 2008), 3rd ed.
32. C. K. Lai, D.-Y. Choi, N. J. Athanasios, K. Yan, W. Y. Chong, S. Debbarma, H. Ahmad, B. J. Eggleton, M. Merklein, and S. J. Madden, "Hybrid Chalcogenide-Germanosilicate Waveguides for High Performance Stimulated Brillouin Scattering Applications," Adv. Funct. Mater. **32**(3), 2105230 (2022).
33. B. Morrison, A. Casas-Bedoya, G. Ren, K. Vu, Y. Liu, A. Zarifi, T. G. Nguyen, D.-Y. Choi, D. Marpaung, S. J. Madden, A. Mitchell, and B. J. Eggleton, "Compact Brillouin devices through hybrid integration on silicon," Optica **4**(8), 847–854 (2017).